1   **Quantitative analysis of fluvial paleohydraulics and intra-channel belt stratal preservation:**

2   **lower Wasatch Formation, Utah, USA**

3   Jesse Pisel[1], David Pyles[2]

4   *[1]Wyoming State Geological Survey, P.O. Box 1347, Laramie WY*

5   *[2]EOG Resources Inc, 600 17th St. Denver CO*

6   **ABSTRACT**

7   This article uses measurements from five fluvial channel belts of the Paleocene lower

8   Wasatch Formation to quantitatively document the transience or persistence of flow velocities

9   recorded in stratigraphy at the bedset scale. We use facies proportions and sedimentary structures

10   coupled with a paleoflow velocity workflow to calculate the mean flow velocity for each bedset.

11   Flow velocity measurements were analyzed using a lattice approach that documents either

12   persistence or transience of mean flow velocities, which, in turn was combined with facies trends

13   to infer perennial and ephemeral flow conditions during the deposition of the channel belt. All

14   five channel belts have significant spatial dependence of mean flow velocities. Based on short-

15   range spatial dependence, we infer perennial flow conditions in both laterally and downstream-

16   accreting channel belts, and ephemeral flow conditions in two downstream-accreting channel

17   belts. The remaining channel belt only has short-range spatial dependence as intra channel-belt

18   erosion has completely destroyed any intermediate and long-range flow velocity dependence

19   within the channel belt. Furthermore, we document that intra channel-belt stratal preservation

20   comes at the expense of basin-scale stratal preservation, meaning high channel migration rates

21   destroy basin-scale architecture (stacking patterns) by channel scouring while preserving intra

22   channel-belt morphodynamics at the bedset scale.

23

INTRODUCTION

External forcing (allogenic) mechanisms such as changes in tectonic uplift, subsidence rates, climate fluctuations, and eustasy have been documented in fluvial stratigraphy and simulated in forward numerical models (Foreman et al., 2012; Allen et al., 2013; Allen et al., 2014). Time series methods have been used to document allogenic signals, including spectral analysis of Fourier and wavelet transforms, as well as autocorrelation functions (Prokoph and Agterberg, 1999; Prokoph and Bilali, 2008; Jerolmack and Paola, 2009). However, recent research documents that internal (autogenic) mechanisms act as a non-linear filter that can destroy allogenic signals if the amplitude and period of the external signal is less than the noise of the sediment transport system (Jerolmack and Paola, 2009). Recognizing allogenic signals in stratigraphy is important for predicting how fluvial systems respond to tectonic, climatic, and eustatic changes. Allogenic signals have been documented at the basin scale (100-1,000 m scale thickness), however few studies have concentrated on the channel-belt and bar scale (1-100 m thick) (e.g. Allen et al., 2014). In this study we use the term bedset, which is a hierarchical term, used to describe stratigraphy composed of smaller beds, is genetically related, similar in areal extent and time span of deposition (Ford and Pyles, 2014), and is comparable to an active barform migrating through an active channel.

Two end-member channel-belt types have been interpreted to document short term (yearly to decadal) climatic signals, perennial and ephemeral. Perennial channel belts are interpreted to document persistent flow conditions, with annual to decadal fluctuations related to seasonality in sediment and water flux (Meinzer, 1923; Fielding et al., 2009). Ephemeral channel belts document transient flow conditions between wet and dry periods (McKee et al., 1967; North and Taylor, 1996). Despite differences in flow conditions and bedforms associated with

47   the two channel belt types, documenting persistence or transience of flow conditions on a

48   decadal to 100 year timescale within ancient fluvial channel belts remains challenging. This

49   study uses cross sections, measured sections, grain-size distributions, lithofacies, and bedset

50   bounding surfaces to document allogenic climate signals within fluvial channel belts.

51   **GEOLOGIC SETTING**

52   The lower Wasatch Formation of the Uinta Basin in eastern Utah contains world class

53   exposures of a low net-sand content fluvial system. The Uinta Basin is a longitudinally

54   asymmetric foreland basin located in northeastern and central Utah (Figure 1A). From the

55   Paleocene through Eocene, flexurally induced subsidence provided accommodation for

56   deposition of the Green River and Wasatch Formations (Figure 1A) (Osmond, 1964). Lacustrine

57   sediments deposited in the center of the basin were surrounded by deltaic and fluvial strata of the

58   Green River and Wasatch Formations; signifying internal drainage (Picard, 1955; Keighley et al.,

59   2002). Paleocurrent directions in the southern outcrops of the Wasatch Formation document

60   fluvial systems flowing north and northeast towards the center of the basin (Ford and Pyles,

61   2014, Pisel et al., 2018) (see paleocurrent rose diagram in Figure 1B). Climatically, the lower

62   Wasatch Formation is interpreted to have been deposited during global hot house conditions

63   (Sewall and Sloan, 2006). Basin-scale studies in the adjacent Piceance basin document hundred

64   thousand year changes in channel belt dimensions and sedimentary structures attributed to

65   climatic fluctuations at the Paleocene-Eocene Thermal Maximum (Foreman et al., 2012).

66   **DATASET AND METHODS**

67   An exceptionally well exposed, strike-oriented outcrop of the lower Wasatch Formation

68   is used to address the goals of this study (Figure 1B). The outcrop is located along the southern

69   margin of the Uinta basin, just west of the modern day Green River (39.352 N, 110.063 W), and

70   is 5 km wide by 300 m thick. The outcrop contains 274 fluvial channel belts, all of which are

71   exceptionally well exposed and accessible. Five channel belts were analyzed in detail. They

72   represent the range of architectural variability in the outcrop and span a range of varying

73   numbers of stories and accretion styles. Using the hierarchical approach of Ford and Pyles

74   (2014) the 5 channel belts were characterized on the basis of bar migration direction as follows

75   (Figure 2): (Channel Belt 1) laterally-accreting multi story, (Channel Belt 2) downstream and

76   laterally accreting multi story, (Channel Belt 3) downstream-accreting single story, (Channel

77   Belt 4) downstream-accreting multi story, (Channel Belt 5) laterally-accreting with erosionally

78   based fine-grained fill multi story, respectively (Figure 2).

79   The following data were collected to address the goals of this study: (1) decimeter-

80   resolution measured sections that qualitatively documents grain-size distributions, sorting,

81   rounding, physical and biogenic sedimentary structures, bedset, story, and element boundaries;

82   (2) high-resolution photo panels; (3) paleocurrent orientations collected from flutes, ripples,

83   cross-strata, channel-belt margin orientations; and (4) laser range finding measurements of

84   element, story, and bar form widths and thicknesses. These data were used to generate further

85   information about the channel belts using the following workflow. First, grain size distributions

86   were calculated from measured sections where grain size was optically measured using hand lens

87   and grain size card. Median grain size (D_{50}) and maximum grain size (D_{90}) are calculated from

88   the distributions for each channel belt (Figure 3A). Cross-sections of the channel belts were

89   created by tracing bedset boundaries in the photo panels and combined with measured sections to

90   constrain grain size and facies type for each bedset. Additionally, measured bar-form heights

91   were used to constrain flow depths for bedsets as bar forms scale to flow depth (Figure 3C).

92   From the field data we calculate the mean slope from all 5 channel belts using the

93   paleoslope reconstruction suspension methods of Lynds et al. (2014). To calculate paleoslope

94   using this method we first we calculate the settling velocity of the coarsest grains in suspension

95   ($w_{s(dmaxs)}$) using the equation from Ferguson and Church (2004):

96
$$w_{s(Dmaxs)} = \frac{gRD_{90}^2}{18\nu + (0.75CgRD_{90}^3)^{1/2}}$$
(1)

97   where g is the acceleration of gravity, R is the specific gravity of the particle in the water, D_{90} is

98   the maximum grain size, ν is the kinematic viscosity of the fluid, and C is a constant equal to 1

99   for typical sand grains. Next we calculate z_0 which is the height at which the velocity goes to

100 zero. To calculate z_0 we use the assumption of Lynds et al. (2014) based on Wiberg and Rubin

101 (1989) that $z_0 = 0.056b$ and b is approximately two times the median bedload grain size $b \approx$

102 $2.0D_{50b}$ which we approximate by substituting D_{90} for D_{50b}. Using z_0 we then calculate the ratio

103 of total boundary stress to skin-friction shear stress:

104
$$F = 1 + \frac{C_d}{2\kappa^2} \frac{h_d}{\lambda} \left[\ln\left[\frac{h_d}{z_0}\right] - 1 \right]^2$$
(2)

105 where C_d is an empirically determined drag coefficient (0.21), κ is von Kármán's constant, h_d is

106 0.3 times flow depth (0.3H), and the dune height-to-length ratio h_d/λ is 0.063 (Lynds et al.,

107 2014). Now that we have calculated $w_{s(Dmaxs)}$ and F we can calculate paleoslope for the lower

108 Wasatch Formation using the following from Lynds et al., (2014):

109

110
$$S = \frac{F(w_{s(Dmaxs)})^2}{g\langle H \rangle}$$
(3)

111 where S is slope, F is the ratio of total boundary shear stress to skin-friction shear stress, $w_{s(dmaxs)}$

112 is the settling velocity of the coarsest grain in suspension, g is gravity, and H is flow depth. The

113 limitations of paleoslope reconstructions have been discussed by Trampush et al. (2014), and

114   Lynds et al. (2014), so now we will now cover the potential for error and how it propagates

115   through this system of equations in our slope calculations.

116   We use Sobol indices to quantitatively understand the sensitivity of the paleoslope

117   estimates. Sobol indices are a normalized decomposition of variance that can be attributed to

118   specific inputs to the model. As Sobol index values for a single input approach 1 they have more

119   fractional variance associated with that variable (Sobol, 2001; Saltelli, 2002; Saltelli et al., 2010

120   ). Meaning that the larger the value, the more influence a particular variable has in the system.

121   We ran 30,000 simulations of paleoslope estimates to calculate Sobol indices for each source of

122   error in the calculation. For 10,000 simulations we varied D_{90} by $\pm 1\phi$ grain size larger and

123   smaller than our observed values. For 10,000 simulations we varied D_{50} by $\pm 1\phi$ grain size larger

124   and smaller than our observed values. And finally for 10,000 simulations we varied flow depth

125   (H) by $\pm 35\%$ of the average flow depth of channel belts in the lower Wasatch Formation

126   (9.1 ± 3.185 m). The resulting first order Sobol indices are as follows 0.8982 (D_{90}), 0.0126 (D_{50}),

127   0.0259 (H). These results document that the maximum grain size and flow depth have first order

128   controls on paleoslope. Total order Sobol indices are 0.9634 (D_{90}), 0.0126 (D_{50}), and 0.0661 (H)

129   respectively, and document weak higher order interactions between the three variables, of which

130   none are significant. Again, the sensitivity analysis was based on an assumed error of $\pm 1\phi$ grain

131   size and 90% variance in flow depth.

132   Now that we have quantitatively documented which variables have first and second order

133   controls, we can calculate paleoslope and associated uncertainty. We use one standard deviation

134   as our uncertainty bounds based on a grain size error of $\pm 1\phi$ for both D_{90} and D_{50}. This

135   uncertainty is based on the assumption that our grain size measurements are within 1ϕ of the

136   mean grain size. We think that this assumption is reasonable as it would be comparable to

137 mistaking coarse sand for fine sand. Additionally, we assume that our flow depth is within 35%

138 (±3.185 m) of the mean channel-belt flow depth (9.1 m) for all measured channel belts in the

139 lower Wasatch (Pisel et al., 2018). From these assumed sources of error, we calculate the

140 paleoslope of the lower Wasatch Formation to be 2.8×10^{-3} with a maximum of 5.4×10^{-3} and a

141 minimum of 1.6×10^{-4}. The mean and lower limits are well within the reasonable bounds

142 discussed by Trampush (2014) while the upper slope estimate is on the edge of what they

143 consider reasonable. Nevertheless, this gives us a place to further investigate paleoflows within

144 the lower Wasatch Formation.

145   Using the mean paleoslope (2.8×10^{-3}) and flow depth measurements for each barform

146 (Figure 3C) we calculate the bed shear stress using the depth-slope product (Leopold et al.,

147 1964):

148 $$\tau_b = \rho g H S \qquad (4)$$

149 where ρ is the density of the fluid, g is gravitational acceleration, H is flow depth, and S is slope.

150 The flow depth is constrained by the amount of relief on the barforms, as they scale to the water

151 surface, and are the most accurate measure of paleo-flowdepth. Next, we substitute in bed shear

152 stress (equation 3) to calculate the shear velocity (Shields, 1936):

153 $$u_* = \sqrt{\frac{\tau_b}{\rho}} \qquad (5)$$

154 where τ_b is the bed shear stress and ρ is the fluid density. Finally, from the shear velocity

155 (equation 4) we calculate the average velocity using the Law of the Wall (von Kármán, 1930):

156 $$u = \frac{u_*}{k}\left(ln\frac{z}{z_0}\right) \qquad (6)$$

157 where z is the height of the velocity measurement, z_0 is the level at which the velocity goes to

158 zero, u_* is the shear velocity, and k is von Kármán's constant. In this study we define z as 6/10ths

159   the height of flow depth to calculate an average flow velocity. Furthermore, we define z_0 as we

160   did during the previous slope calculations.

161   We further investigate error in our flow velocity calculations using Monte Carlo

162   simulations to explore the distributions of potential flow velocities in the lower Wasatch

163   Formation. Specifically we assume that the error in the maximum grain size, mean grain size,

164   flow depth, and slope is normally distributed, centered on our field measured values, and that the

165   standard deviations are the same as those used in the sensitivity analysis. Given these

166   assumptions, the simulations proceed as follows: (1) select a bedset in the channel belt, (2) for

167   the selected bedset calculate the paleoflow velocity distribution from the mean paleoflow

168   velocity and its standard deviation, (3) randomly choose a velocity value from the velocity

169   distribution for the bedset, (4) select the next bedset and repeat steps 1-3, (5) repeat this process

170   99 times for each channel belt before moving to the next channel belt and repeating steps 1-5.

171   This builds a robust dataset with 35,900 data points for flow velocity and flow depth.

172   Next we visualize how the uncertainty in flow velocity changes with flow depth as a 2D

173   kernel density estimate (Figure 4). Note that as flow depth increases, the variance in the flow

174   velocity increases as well. We attribute this to the increase of variance in the slope estimate as

175   flow depth increases. This is exactly what Trampush et al. (2014) discuss, that the error in flow

176   depth estimates propagates through to the slope estimate. Here we document that flow depth

177   uncertainty also propagates through to velocity calculations as well. Figure 4 documents the

178   range of flow velocities that we generated from the Monte Carlo simulations for the channel

179   belts in the lower Wasatch. Areas of higher density (lighter colors) infer a higher confidence in

180   the calculation. Now that we have discussed how we calculate paleoflow velocities and sources

181   of error within the systems of equations we will further discuss the analytical methods we used to

182   spatially evaluate the data.

183   Spatial persistence and transience of mean flow velocity were quantified using spatial

184   statistics and lattice methods. Lattice data are discrete, with each region represented by an

185   average of the data. In this study we define regions by bedsets, and assign the mean-flow

186   velocity to each. We define spatial neighborhoods for each bedset using row standardized

187   weights, meaning that bedsets in contact with one another (linked) are spatially related. Beyond

188   adjacent bedsets, we evaluated spatial autocorrelation of mean flow velocity at increasing, non-

189   adjacent bedset lags using Moran's *I*. Bedset lag spatial autocorrelation simply increases the

190   neighborhood structure to include beds that are not directly in contact with one another which

191   documents long-range spatial trends. Spatial autocorrelation, which is the cross-correlation of a

192   region with its neighbors, is calculated using Moran's *I*:

193
$$I = \frac{n}{\sum\limits_{i=1}^{n}\sum\limits_{j=1}^{n} w_{ij}} \frac{\sum\limits_{i=1}^{n}\sum\limits_{j=1}^{n} w_{ij}(y_i - \bar{y})(y_j - \bar{y})}{\sum\limits_{i=1}^{n}(y_i - \bar{y})^2} \tag{7}$$

194   where y_i is the *i*-th observation, y_j is the *j*-th observation $\bar{y}$ is the global mean flow velocity and

195   W_{ij} is the spatial weight of the link between regions *i* and *j* defined above using row standardized

196   binary weights (Moran, 1950). The expected value of Moran's *I* under the null hypothesis of no

197   spatial dependence is:

198
$$E(I) = \frac{-1}{N-1} \tag{8}$$

199   where *N* is the number of locations. To test for spatial autocorrelation using Moran's *I,* we use

200   Monte Carlo simulations. In this test, 99 Monte Carlo simulations were run for each channel belt.

201   Values for each region are randomly reassigned to a new region and Moran's *I* is calculated for

202   each simulation. Calculated Moran's *I* is compared to the distribution of Moran's *I* from the

203   Monte Carlo simulations. If the observed value of *I* is outside the distribution generated from the

204   simulations (p<0.05), there is significant evidence for spatial autocorrelation. Moran's *I* ranges

205   from -1 to 1, where negative values document negative correlation (transience), and positive

206   values document positive correlation (persistence) and values near 0 document spatial

207   independence.

208   **RESULTS**

209   **<u>Velocities</u>**

210   All five channel belts document increasing mean flow velocity with increasing flow depth as we

211   expect given equation 5. In all five channel belts, a majority of the calculated variance stems

212   from uncertainty in slope estimates. A slope of $2.8x10^{-3} \pm 2.5x10^{-3}$ results in the following mean

213   flow velocities in meters per second: Channel Belt 1 0.55±0.29, Channel Belt 2 0.20±0.11,

214   Channel Belt 3 0.28±0.14, Channel Belt 4 0.40±0.21, and Channel Belt 5 0.45±0.23. If we

215   exclude the slope variance and only use flow depth and grain size variance for the velocity

216   calculations, our standard deviation is half of what we calculate with the slope variance (Table

217   1). From the average flow velocities for each bedset, we calculate the spatial autocorrelation

218   (Moran's *I*) for an increasing numbers of bedset lags.

219   **<u>Moran's *I*</u>**

220   For a bedset lag of 1, all five characters belts have documented positive spatial

221   autocorrelation (or similarity) of mean flow velocity using Moran's *I* (Figure 5a). As we increase

222   the region neighborhoods, or distance between bedsets, we document positive spatial

223   autocorrelation up to 2 bedset lags for all the channel belts (Figure 5a). Meaning the mean flow

224   velocities in all the channel belts are locally similar from bedset to bedset both vertically and

225   laterally. Channel Belts 3 and 4 have positive spatial correlation at bedset lags of 3, while the

226   mean flow velocity for Channel Belts 1, 2, and 5 is spatially independent and remains that way

227   through 4 bedset lags. At bedset lags of 5 and 6, Channel Belts 1-4 have negative spatial

228   autocorrelation of mean flow velocity (Figure 5b-e). This means mean flow velocities in

229   intermediate bedsets, both vertically and laterally, are dissimilar. Channel Belt 5 has no

230   correlation for any bedset lags higher than 2 (Figure 5f), meaning that mean flow velocities for

231   all bedsets are spatially independent or different.

232   In all 5 channel belts the diagnostic sedimentary structures associated with high and low

233   flow regimes coupled with facies proportions provide further information into the meaning of the

234   Moran's *I* results. Specifically, spatial persistence of flow velocity, low facies diversity, and low

235   flow regime associated facies are interpreted to be characteristic of perennial deposits. In

236   contrast, spatial transience of flow velocity, high facies diversity, and high flow regime

237   associated facies are interpreted to be characteristic of ephemeral deposits.

238   We interpret the short-range, positive autocorrelation, facies, and bar migration

239   orientation in Channel Belts 1 and 5 to collectively record short term stasis in flow velocity. Both

240   of these channel belts migrated solely laterally, which is interpreted to have preserved the

241   depositional processes. From the facies proportions, we interpret Channel Belt 5 to document

242   ephemeral deposits, as the facies record high flow regime conditions within the channel belt.

243   Additionally in Channel Belt 5 we interpret that the spatial independence of flow velocity at

244   intermediate and long distances documents the deposition and subsequent erosion of bars in a

245   random manner, resulting in the spatial independence of flow velocity.

246   Channel Belt 1 is interpreted to document perennial deposits as the facies are

247   predominantly low flow regime associated facies (e.g. facies F3, F4, F5) and do not vary within

248   the channel belt. Therefore, we infer the intermediate-range transience in flow velocity is the

249   result of periods of high and low flow velocity as the channel belt laterally migrated.

250   We interpret the short-range positive autocorrelation, intermediate-range negative

251   autocorrelation, facies, and bar migration orientation in Channel Belts 3 and 4 to record short

252   term stasis in flow velocity along with long term transience in flow velocity. Furthermore, using

253   facies proportions, we interpret Channel Belt 3 to document ephemeral deposits as the facies

254   record high flow regime (e.g. facies F8, F9, F10) and vary significantly within the channel belt.

255   In Channel Belt 3, we interpret the intermediate-range transience of flow velocity is due to

256   decreasing flow depth related to rapid filling of the channel belt. A majority of facies in Channel

257   Belt 3 (e.g. Facies F9 and F10) are characteristic of high deposition rates that are common in

258   ephemeral deposits, and support the hypothesis of a rapidly filling channel belt (Figure 5c).

259   Channel Belt 4 is interpreted to document perennial deposits as the facies are

260   predominantly low flow regime associated facies (e.g. facies F3, F4, F5) and have little

261   variability within the channel belt. Therefore, we infer the intermediate and long-range

262   transience in flow velocity is due to alternating periods of high and low flow velocity rather than

263   rapid infilling of the channel belt.

264   We interpret Channel Belt 2 documents perennial deposits; the majority of the facies are

265   diagnostic of lower flow regime conditions which are interpreted by North and Taylor (1996) to

266   record low discharge and low flow velocity conditions (Figure 5b). Facies in Channel Belt 4

267   document both high and low flow conditions, but is primarily facies that are interpreted to

268   document low flow regime (Figure 5e). Additionally, the short-range persistence and

269   intermediate range transience of flow velocities document periods of alternating high and low

270 flow. Therefore, we interpret this channel belt to be a combination of perennial and ephemeral

271 flow conditions.

DISCUSSION

273 The paleoflow velocities and associated error is minimized by minimizing the error in the

274 paleoslope calculation. When we constrain the slope error, we minimize the variance in flow

275 estimates by over half. However, the same variables that contribute to the error in the slope

276 estimate are also used in the velocity calculation, so minimizing error in the field measurements

277 has a two-fold effect of constraining slope, and velocity calculations. Further work is needed to

278 compare measured velocity data from modern systems and the calculated slope and velocity

279 from grain size and flow depth. However, we note that Moran's I values are rather insensitive to

280 the variance in flow velocity in our Monte Carlo simulations and give us quantitative bounds for

281 Moran's I for each bedset (Figure 4).

282 From the spatial autocorrelation results, we interpret the rate of lateral migration within

283 laterally-accreting channel belts, to be proportional to preservation potential of the subjacent

284 bars. Furthermore, we interpret that the rate of in channel belt aggradation within downstream-

285 accreting channel belts is also proportional to the preservation potential of subjacent bars.

286 Results from this study suggest intra-channel belt preservation of allogenic signals to be opposite

287 those of basin-scale channel-belt stacking patterns documented by Straub and Esposito (2013).

288 At the bar scale, if a channel moves laterally quickly the underlying basin-scale strata is

289 removed, but the intra-channel belt architecture is preserved. Conversely, if a channel doesn't

290 migrate laterally, the basin-scale channel-belt stacking pattern is better preserved. However, if

291 downstream migrating bars aggrade quickly enough, both the basin-scale and intra-channel belt

292 architecture is preserved. Therefore there is a scale-dependent tradeoff in signal preservation

293   from intra-channel belt architecture to basin-scale stacking patterns. This concept provides

294   insight into the scales that future studies should consider when attempting to resolve external

295   signals. Systems with deep laterally-migrating channel belts should be considered ideal when

296   attempting to resolve signals at the intra-channel belt scale, while systems with shallow

297   downstream-migrating channel belts should be considered ideal to study when attempting to

298   resolve basin-scale signals. Furthermore, the spatial relationships between some bedsets are non-

299   random, and are related to both external controls and hydrologic conditions

300   **CONCLUSION**

301   We interpret perennial and ephemeral fluvial systems in the lower Wasatch Formation

302   based on spatial dependence and facies types. Perennial rivers have short range positive

303   autocorrelation, intermediate and long range negative autocorrelation, and are composed of low-

304   flow regime bedforms. Ephemeral rivers have both short range positive autocorrelation, long

305   range negative autocorrelation, and contain sedimentary structures and facies indicative of upper

306   flow regime and high deposition rates. External signals that are completely masked by deposition

307   and subsequent erosion are characterized by no spatial dependence at all but short distances.

308   However, facies proportions and sedimentary structures document facies associated with both

309   perennial and ephemeral rivers.

310   This article quantitatively documents a paleoflow velocity calculation method and the

311   associated sources and propagation of error through the system of equations. Additionally we

312   document perennial and ephemeral signals within fluvial channel belts. We use a workflow to

313   calculate mean flow velocity and associated error for each bedset. Using Moran's *I*, facies

314   patterns, and migration orientations, we document spatial dependence and independence in mean

315   flow velocity. We interpret short and long-range spatial dependence and facies types to

316 differentiate between rapid filling of ephemeral channel belts, and the fluctuations of flow

317 velocity of perennial channel belts. Furthermore, we document that repeated deposition and

318 erosion of barforms results in local spatial dependence, but intermediate and long-range

319 independence of flow velocities. Concepts developed in this study provide context from a world

320 class fluvial outcrop to previous tank and numerical studies on the preservation of external

321 signals, and are applicable to both modern and ancient fluvial systems around the globe.

322 **APPENDIX OF VARIABLES**

323 v kinematic viscosity of water

324 ρ density of water

325 τ_b bed shear stress

326 C constant equal to 1

327 C_d drag coefficient

328 D_{90} maximum grain size

329 $E(I)$ expected value of Moran's I

330 F ratio of boundary stress to skin-friction shear stress

331 g gravitational acceleration

332 H flow depth

333 h_d 0.3 times flow depth

334 h_d/λ dune height-to-length ratio

335 κ von Kármán's constant

336 N number of bedsets

337 R specific gravity of a particle in water

338 S slope

339   u_* shear velocity

340    $w_{s(Dmaxs)}$ settling velocity of coarsest grain in suspension

341   W_{ij} spatial weights

342    $\bar{y}$ global mean flow velocity

343   y_i i-th observation in Moran's I

344   y_j j-th observation in Moran's I

345   z_0 height above the bed at which the velocity goes to zero

346   z height of the velocity measurement,

347

357 **REFERENCES CITED**

358 Allen, J. P., Fielding, C. R., Gibling, M. R., & Rygel, M. C. (2014). Recognizing products of

359   palaeoclimate fluctuation in the fluvial stratigraphic record: An example from the

360   Pennsylvanian to Lower Permian of Cape Breton Island, Nova Scotia. *Sedimentology*,

361   *61*(5), 1332–1381.

362   Allen, J. P., Fielding, C. R., Rygel, M. C., & Gibling, M. R. (2013). Deconvolving signals of

363   tectonic and climatic controls from continental basins: an example from the late

364   Paleozoic Cumberland Basin, Atlantic Canada. *Journal of Sedimentary Research*, *83*(10),

365   847–872.

366   Fielding, C. R., Allen, J. P., Alexander, J., & Gibling, M. R. (2009). Facies model for fluvial

367   systems in the seasonal tropics and subtropics. *Geology*, *37*(7), 623–626.

368   Ford, G. L., & Pyles, D. R. (2014). A hierarchical approach for evaluating fluvial systems:

369   Architectural analysis and sequential evolution of the high net-sand content, middle

370   Wasatch Formation, Uinta Basin, UtahGeohorizon. *AAPG Bulletin*, *98*(7), 1273–1304.

371   Foreman, B. Z., Heller, P. L., & Clementz, M. T. (2012). Fluvial response to abrupt global

372   warming at the Palaeocene/Eocene boundary. *Nature*, *491*(7422), 92.

373   Herman, J., & Usher, W. (2017). SALib: an open-source Python library for sensitivity analysis.

374   *The Journal of Open Source Software*, *2*(9).

375   Hunter, J. D. (2007). Matplotlib: A 2D graphics environment. *Computing in Science &*

376   *Engineering*, *9*(3), 90–95.

377   Jerolmack, D. J., & Paola, C. (2010). Shredding of environmental signals by sediment transport.

378   *Geophysical Research Letters*, *37*(19).

379   Keighley, D., Flint, S., Howell, J., Andersson, D., Collins, S., Moscariello, A., & Stone, G.

380   (2002). Surface and Subsurface Correlation of the Green River Formation in Central Nine

381   Mile Canyon, SW Uinta Basin, Carbon and Duchesne Counties, East-Central Utah (MP-

382   02-1).

383   Leopold, L. B., & Wolman, M. G. (n.d.). Miller] P. 1964. Fluvial processes in geomorphology.

384   *San Francisco, California, Freeman*, *522*, 135–163.

385 Lynds, R. M., Mohrig, D., Hajek, E. A., & Heller, P. L. (2014). Paleoslope reconstruction in

386   sandy suspended-load-dominant rivers. *Journal of Sedimentary Research*, *84*(10), 825–

387   836.

388 McKee, E., Crosby, E. t, & Berryhill Jr, H. (1967). Flood deposits, Bijou Creek, Colorado, June

389   1965. *Journal of Sedimentary Research*, *37*(3).

390 McKinney, W. (2010). Data structures for statistical computing in python (Vol. 445, pp. 51–56).

391   Presented at the Proceedings of the 9th Python in Science Conference, Austin, TX.

392 Meinzer, O. E. (1923). Outline of ground-water hydrology. *US Geological Survey Water Supply*

393   *Paper*, *494*, 5.

394 Moran, P. A. (1950). Notes on continuous stochastic phenomena. *Biometrika*, *37*(1/2), 17–23.

395 North, C. P., & Taylor, K. S. (1996). Ephemeral-fluvial deposits: integrated outcrop and

396   simulation studies reveal complexity. *AAPG Bulletin*, *80*(6), 811–830.

397 Oliphant, T. E. (2006). *A guide to NumPy* (Vol. 1). Trelgol Publishing USA.

398 Osmond, J. C. (1964). Tectonic history of the Uinta basin, Utah.

399 Pérez, F., & Granger, B. E. (2007). IPython: a system for interactive scientific computing.

400   *Computing in Science & Engineering*, *9*(3).

401 Picard, M. D. (1956). Summary of Tertiary oil and gas fields in Utah and Colorado. *AAPG*

402   *Bulletin*, *40*(12), 2956–2960.

403 Pisel, J. R., Pyles, D. R., & Kirschbaum, M. A. (2018). The influence of lateral topographic

404   confinement on fluvial channel-belt clustering, compensation and connectivity–lower

405   Wasatch Formation and Dakota Sandstone, Utah, USA. *Sedimentology*, *65*(2), 597–619.

406 Prokoph, A., & Agterberg, F. P. (1999). Detection of sedimentary cyclicity and stratigraphic

407   completeness by wavelet analysis: an application to late Albian cyclostratigraphy of the

408   Western Canada sedimentary basin. *Journal of Sedimentary Research*, *69*(4).

409   Prokoph, A., & El Bilali, H. (2008). Cross-wavelet analysis: a tool for detection of relationships

410   between paleoclimate proxy records. *Mathematical Geosciences*, *40*(5), 575–586.

411   Saltelli, A. (2002). Making best use of model evaluations to compute sensitivity indices.

412   *Computer Physics Communications*, *145*(2), 280–297.

413   Saltelli, A., Annoni, P., Azzini, I., Campolongo, F., Ratto, M., & Tarantola, S. (2010). Variance

414   based sensitivity analysis of model output. Design and estimator for the total sensitivity

415   index. *Computer Physics Communications*, *181*(2), 259–270.

416   Sewall, J. O., & Sloan, L. C. (2006). Come a little bit closer: A high-resolution climate study of

417   the early Paleogene Laramide foreland. *Geology*, *34*(2), 81–84.

418   Shields, A. (1936). Application of similarity mechanics and turbulence research on shear flow.

419   *Mitteilungen Der Preußischen Versuchsanstalt Für Wasserbau (in German)*, (26).

420   Sobol, I. M. (2001). Global sensitivity indices for nonlinear mathematical models and their

421   Monte Carlo estimates. *Mathematics and Computers in Simulation*, *55*(1–3), 271–280.

422   Trampush, S., Huzurbazar, S., & McElroy, B. (2014). Empirical assessment of theory for

423   bankfull characteristics of alluvial channels. *Water Resources Research*, *50*(12), 9211–

424   9220.

425   Von Kármán, T. (1931). Mechanical similitude and turbulence.

426   Wiberg, P. L., & Rubin, D. M. (1989). Bed roughness produced by saltating sediment. *Journal of*

427   *Geophysical Research: Oceans*, *94*(C4), 5011–5016.

428   **FIGURE CAPTIONS**

429   Figure 1. (A) Map showing the location of the Uinta Basin and bounding structures. Inset is a

430   chronostratigraphic chart of the Uinta Basin. The lower Wasatch Formation lies between the

431   Flagstaff Limestone and middle Wasatch Formation and is the focus of this study. (B)

432   Photopanel of the field area showing the locations of the 274 channel belts. The five used in this

433   study are labeled 1-5 and are highlighted by the colored boxes.

434

435   Figure 2. Stratigraphic cross sections through the five channel belts within the lower Wasatch

436   Formation used in this study. Sediment transport is into the page for all channel belts. Bedsets

437   are colored according to the dominant facies within the bedset. Brown and green colors reflect

438   facies with clay-sized sediment, while yellow and orange are facies with silt and sand. Facies

439   proportions by area are documented in the pie charts next to each channel belt.

440

441   Figure 3. (A) Grain-size distributions for the channel belts used in this study. Grain-size

442   measurements were made throughout the measured sections, and across the outcrop face. (B)

443   Box and whisker plots of mean flow velocities calculated for bedsets in channel belts. (C) Box

444   and whisker plots of flow depths measured from bar-form thicknesses within the channel belts.

445

446   Figure 4. Two-dimensional kernel density estimate plot of flow velocity and flow depth for all

447   Monte Carlo simulations. Darker colors are areas with fewer points and lighter colors have

448   higher density of points. The velocity and flow depth for each bedset in the five documented

449   channel belts in the lower Wasatch Formation are plotted above to visualize alignment of the

450   variance with the mean values.

451

452   Figure 5. (A)Spatially lagged Moran's I values for channel belts in the lower Wasatch

453   Formation. Increasing the neighborhood structure to include bedsets not directly in contact with

454 one another documents both short and long-range changes in spatial dependence. (B-F) Spatially

455 lagged Moran's *I* values for all documented channel belts in the lower Wasatch Formation with

456 boxplots documenting the variance of Moran's *I* due to variance in flow velocity calculations

457 caused by error propagation from field measurements.

458

459 Table 1. Comparison of variance in mean flow velocity with and without variance in slope for

460 each channel belt. When variance in slope is removed from the error propagation, the standard

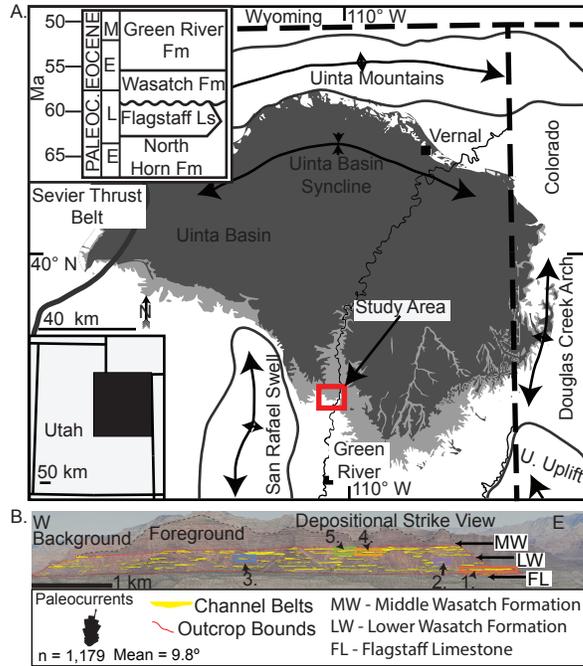461 deviation of flow velocity is cut in roughly half.

Figure 1.

A.

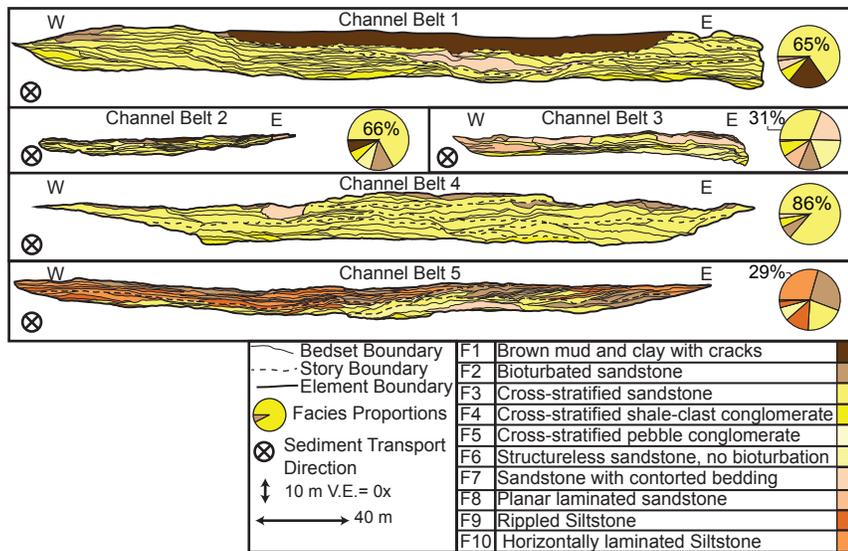| Ma				
50	EOCENE	M	Green River Fm	
55		E	Wasatch Fm	
60	PALEOC.	L	Flagstaff Ls	
65		E	North Horn Fm	

Wyoming   110° W

Uinta Mountains

Vernal

Colorado

Uinta Basin Syncline

Sevier Thrust Belt

Uinta Basin

40° N

40 km

N

Utah

50 km

San Rafael Swell

Study Area

Green River

110° W

Douglas Creek Arch

U. Uplift

B. W   Depositional Strike View   E

Background   Foreground   5. 4.   MW
                                         LW
1 km   3.   2. 1.   FL

Paleocurrents   Channel Belts   MW - Middle Wasatch Formation
                 Outcrop Bounds   LW - Lower Wasatch Formation
n = 1,179 Mean = 9.8°   FL - Flagstaff Limestone

Figure 2.

	F1	Brown mud and clay with cracks
	F2	Bioturbated sandstone
	F3	Cross-stratified sandstone
	F4	Cross-stratified shale-clast conglomerate
	F5	Cross-stratified pebble conglomerate
	F6	Structureless sandstone, no bioturbation
	F7	Sandstone with contorted bedding
	F8	Planar laminated sandstone
	F9	Rippled Siltstone
	F10	Horizontally laminated Siltstone

Bedset Boundary
Story Boundary
Element Boundary
Facies Proportions
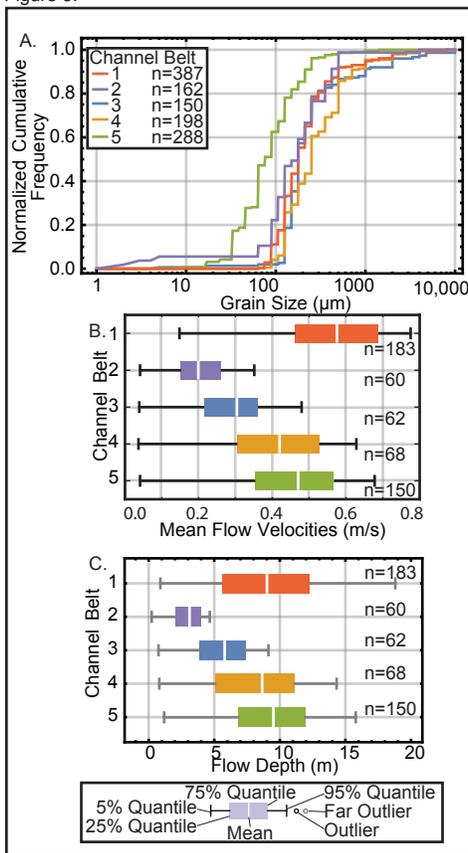Sediment Transport Direction
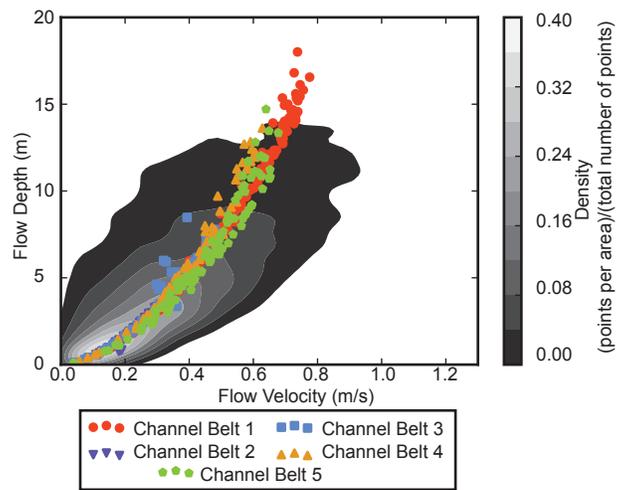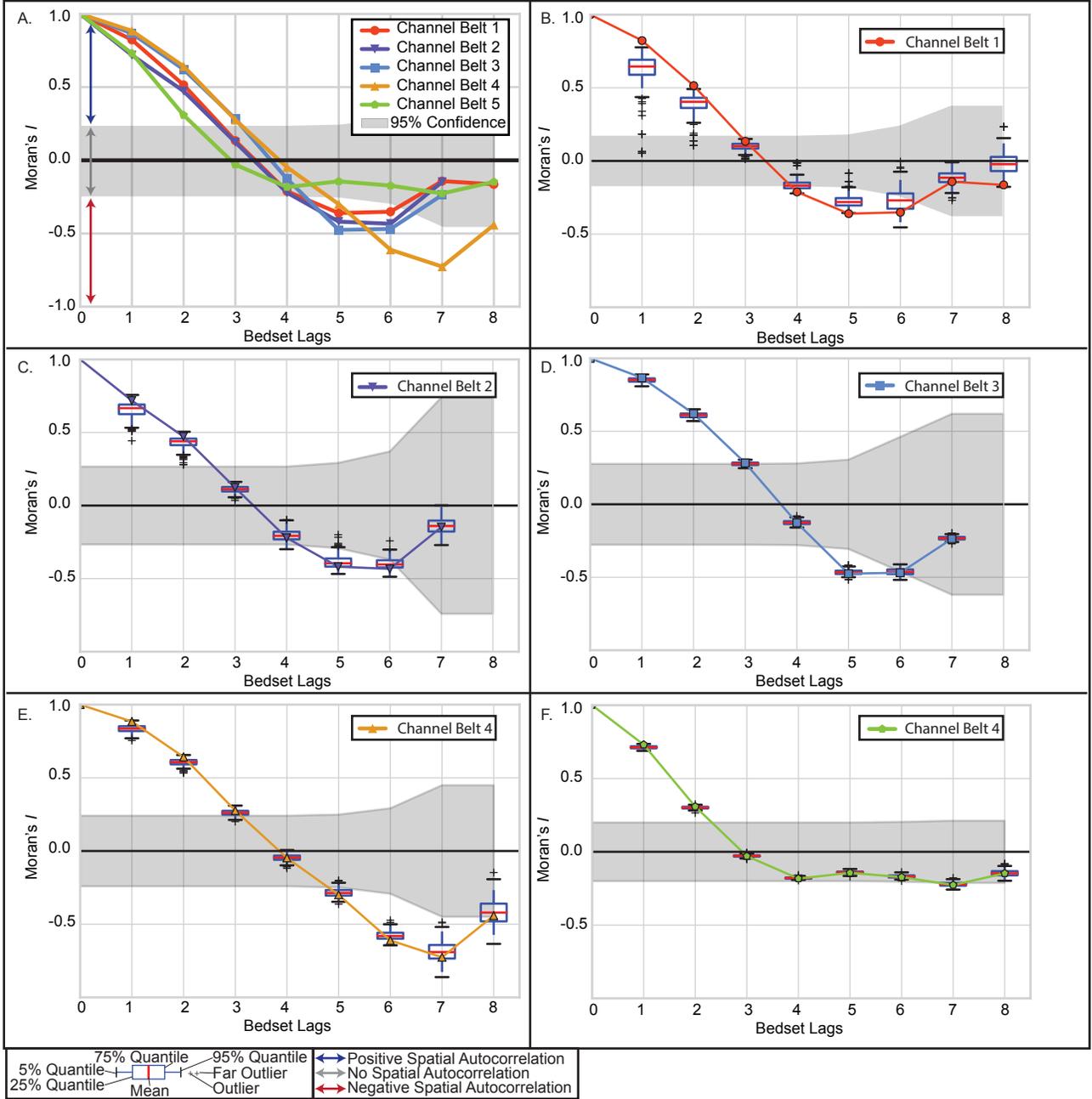10 m V.E.= 0x
40 m

Figure 3.

Figure 4.

Figure 5.

Table 1.

Channel Belt	Mean Flow Velocity with Slope Variance (m/s)	Mean Flow Velocity Standard Deviation with Slope Variance (m/s)	Mean Flow Velocity without Slope Variance (m/s)	Mean Flow Velocity Standard Deviation without Slope Variance (m/s)
1	0.55	0.29	0.55	0.13
2	0.2	0.11	0.2	0.045
3	0.28	0.14	0.28	0.06
4	0.4	0.21	0.4	0.09
5	0.45	0.11	0.45	0.09